Journal of Petroleum Science and Engineering 201 (2021) 108476

Contents lists available at ScienceDirect

Journal of Petroleum Science and Engineering

journal homepage: http://www.elsevier.com/locate/petrol

Seismic identification of tight-oil reservoirs by using 3D rock-physics templates

Mengqiang Pang [a], Jing Ba [a,*], J.M. Carcione [a,b], Lin Zhang [a], Rupeng Ma [a], Yijun Wei [a]

[a] School of Earth Sciences and Engineering, Hohai University, Nanjing, 211100, China
[b] National Institute of Oceanography and Applied Geophysics – OGS, Trieste, Italy

ARTICLE INFO

Keywords:
Tight-oil reservoir
3D rock-physics template
Crack
Clay content
Triple-porosity theory
Attenuation

ABSTRACT

Tight-oil reservoirs are classified as unconventional hydrocarbon resources, having a complex system of pores and cracks and low porosity/permeability. A good pore-crack connectivity is required for hydrocarbon production, but clay minerals filling the pores and throats may hinder the fluid migration. Thus, the combined effects of the pore-crack network and the presence of clay are the main factors controlling the reservoir properties and its storage capacity. In this study, a suite of cores was collected from a reservoir located in the north of the Songliao Basin (China), and establish their microstructure by scanning electron microscopy. Then, ultrasonic experiments were performed under in-situ conditions to analyze the influence of clay minerals and porosity on the elastic waves. The triple-porosity, differential-effective-medium and self-consistent theories were used to calculate the stiffness moduli by considering the effects of pores, cracks and clay minerals, and to analyze the influence of these reservoir properties on the P-wave attributes. According to attenuation, acoustic impedance and phase-velocity ratio, a multi-scale 3D rock-physics template was established. By using the ultrasonic, sonic-log and seismic data, the templates were calibrated and then the reservoir characteristics were estimated. Two 2D seismic lines were considered and the corresponding predicted reservoir properties were compared to the well-log data and the actual production reports, showing that the porosity and clay content predictions are consistent with these data, and that the oil production areas are all located within the high-cracked porous zones. The 3D rock-physics templates can effectively estimate the distribution of high-quality tight-oil reservoirs.

1. Introduction

With the increase in petroleum consumption and the exhaustion of conventional reservoirs (e.g., Yan et al., 2011; Liu et al., 2019; Yu et al., 2020), the exploration of tight-oil reservoirs is increasingly taken into consideration (Zhou et al., 2019). Tight oil is trapped in unconventional resources with low permeability and porosity, widely distributed over the world (Li et al., 2020). Since the development of the Bakken Formation in North America in 1987, the success of shale-gas exploration technology has opened up a new prospect for tight-oil resources development (Li et al., 2017). These reservoirs are widely distributed in the Bohai, Songliao, Sichuan, Junggar, and Ordos basins of China, and have great petroleum potential (Yu et al., 2020). Tight-oil resources are expected to play a significant role on China's hydrocarbon industry (Li et al., 2020).

Tight-oil rocks include tight sandstones, siltstones and carbonates with silt or clay, which have small pore-throat diameters, high clay content and a complex crack structure (Ma et al., 2019, 2020). P-wave velocity is highly dependent on the pore system (Xu and Payne, 2009), such that different pore types can cause up to a 40% variation in velocity at the same total porosity. Thus, the pore structure (shape, size and connectivity) is the main factor affecting the physical properties of a reservoir (Sakhaee-Pour and Bryant, 2014; Xiao et al., 2018), as also has been shown in the other studies (Cheng et al., 2019; Ba et al., 2019). The microstructure of reservoir rocks significantly affects the elastic properties (Zhang et al., 2019).

Hence, the crack structure significantly affects the fluid flow properties of the tight-oil reservoirs (Nelson, 2001; Sun et al., 2014; Benaafi et al., 2019; Hu et al., 2020). Recent works have analyzed the elastic attributes of the rocks containing cracks (Crampin and Bamford, 1977; Gurevich et al., 2009; Smith et al., 2009; Zhang et al., 2019). Pang et al. (2020) built a multi-scale rock-physics model to estimate the microcrack porosity in deep carbonate resources. An additional factor, other than cracks, is clay minerals filling the pores and throats, that prevent the

* Corresponding author.
E-mail address: jba@hhu.edu.cn (J. Ba).

https://doi.org/10.1016/j.petrol.2021.108476
Received 24 August 2020; Received in revised form 20 January 2021; Accepted 25 January 2021
Available online 4 February 2021

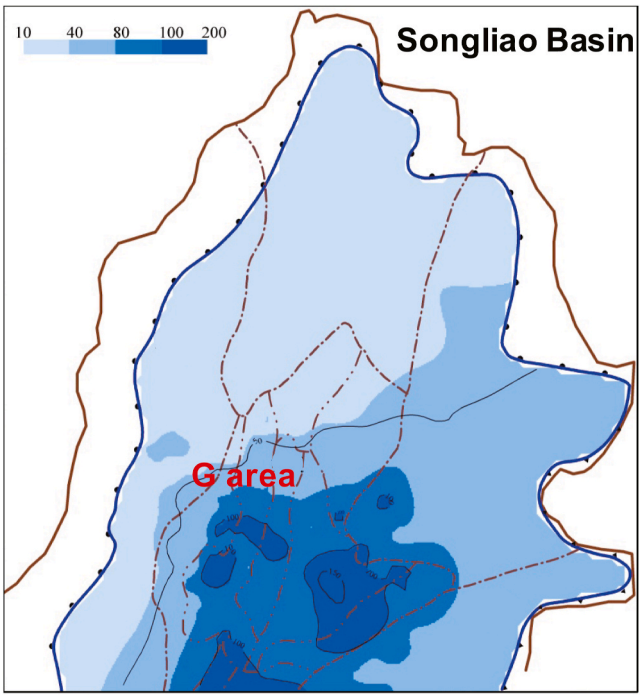

Fig. 1. Thickness distribution of the mudstone (TOC > 2%) of the Qingshankou Formation in Northern Songliao Basin. The G depression area is shown.

fluid migration (Nelson, 2009; Walderhaug et al., 2012; Stroker et al., 2013; Xiao et al., 2018; Xi et al., 2019). Tutuncu et al. (1994) studied the effects of clay content, porosity and pressure on the elastic wave velocities and attenuation in the salt-saturated tight sandstones based on ultrasonic experiments. The results showed that the clay softens the bonds between the grains, resulting in a lower wave velocity. Based on scanning electron microscopy (SEM) and nuclear magnetic resonance (NMR) methods, Xiao et al. (2018) found that when the clay content increases, the pore-volume change is negligible, but the permeability decreases significantly.

Rock-physics templates (RPTs) establish a link between the reservoir microstructural properties and the seismic attributes (Odegaard and Avseth, 2004; Gupta et al., 2012; Nicolás-López and Valdiviezo-Mijangos, 2016). Classical 2D RPTs generally utilize phase-velocity ratio (V_P/V_S) and acoustic impedance to relate the reservoir lithology, porosity and saturation to the wave response (Andersen et al., 2009; Carcione and Avseth, 2015; Tucovic and Gegenhuber, 2017; Das et al., 2019). Golikov et al. (2012) analyzed the heterogeneity and anisotropy of Paleocene shale reservoirs by comparing the velocities of deviated and vertical wells in the North Sea, and established RPTs to explain variations in reservoir fluid and porosity. Tan et al. (2020) analyzed the rock characteristics based on ultrasonic experiments on the core samples, and built a brittleness RPT of tight-oil reservoirs by using equivalent-medium models.

In applying RPTs to the tight-oil reservoirs, the pore-crack structure and the effects of clay minerals must be considered. For this purpose, the SEM technology and ultrasonic experiments were combined to analyze the structure and physical characteristics of the rock samples in this study. Then, on the basis of the equivalent-medium theory and the triple-porosity equation (Zhang et al., 2017), a tight-oil rock-physics

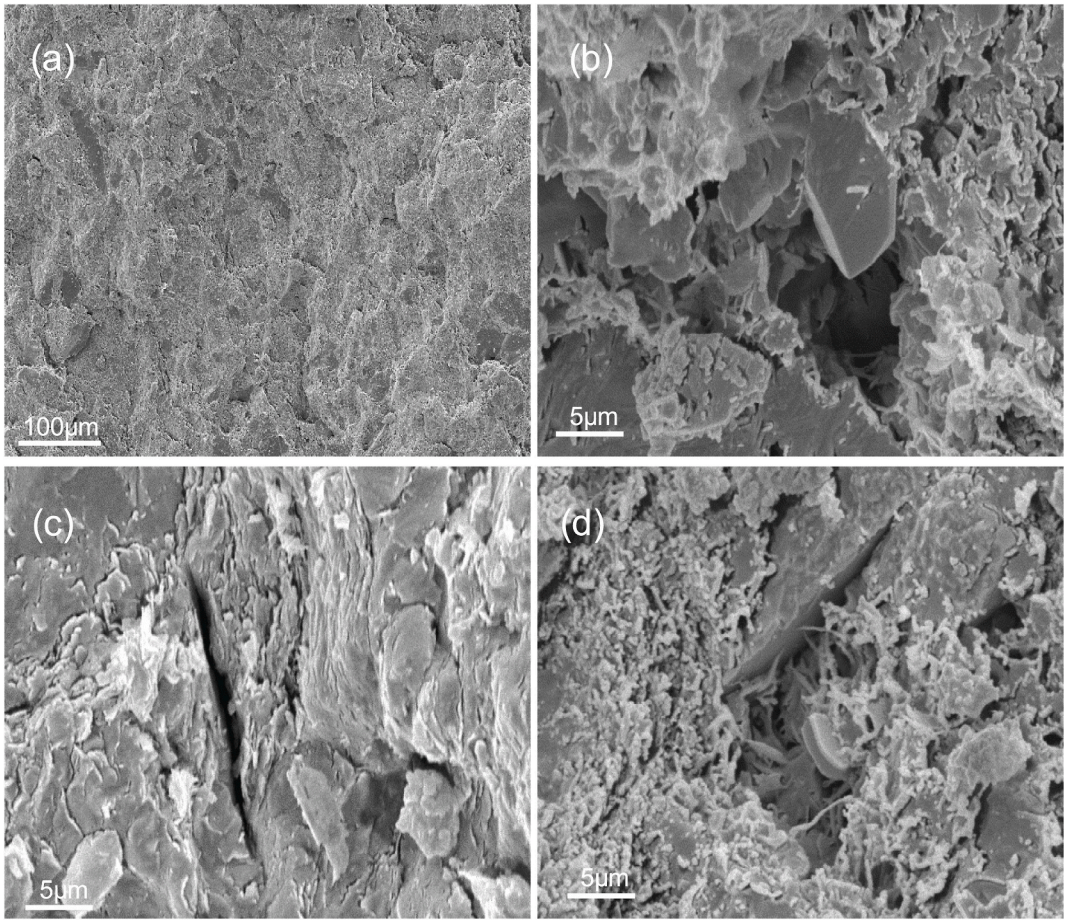

Fig. 2. SEM photographs showing (a) rock particles, (b) enlarged: intergranular pores, (c) cracks, and (d) illite minerals filling the pores.

Table 1
Physical properties of the samples.

Sample	A	B	C	D	E	F	G	H	I	J	K	L
Lithology	Muddy Siltstone	Muddy Siltstone	Siltstone	Muddy Siltstone	Siltstone	Siltstone	Siltstone	Siltstone	Siltstone	Muddy Siltstone	Siltstone	Siltstone
Porosity (%)	2.88	4.60	5.20	5.56	5.60	5.79	5.80	6.45	10.87	12.75	13.09	13.97
Permeability (mD)	0.0045	0.38	0.019	0.011	0.017	0.035	0.02	0.097	0.39	0.17	0.08	0.084
Dry-rock density (g/cm^3)	2.61	2.56	2.58	2.53	2.52	2.41	2.55	2.38	2.29	2.3	2.28	2.26
Clay content (%)	2.8	8.2	1.9	12.5	2.4	3.9	3	5.5	5.5	4.4	5.5	5.5

model was established. Reported theories and experiments show that the crack system has a strong effect on wave dispersion and attenuation (Chapman, 2003; Carcione et al., 2013; Ba et al., 2019; Ma et al., 2019). Thus, the attenuation ($1/Q$, inverse quality factor, also called dissipation factor) was used to build the 3D rock-physics templates for the tight-oil reservoirs, which quantitatively describe the relationship between reservoir properties and wave attributes. The calibrations of the templates were performed by using the laboratory, log and seismic data, to estimate the equant porosity, crack porosity and clay content, and map the distribution of the high-quality reservoirs.

2. Ultrasonic measurements

2.1. Reservoir characteristics

The studied reservoir is located in the G area of the depression zone in the north of the Songliao Basin, China (see Fig. 1). Recently, the huge potential tight-oil resources have been found in Qingshankou Formation in this area (Shi et al., 2015). The mentioned formation is divided into three subsections including Qingshankou 1, 2 and 3 (Ma et al., 2019). In Qingshankou 2 section, the high-quality source rocks have been developed, with wide distribution and good continuity, where there is a good source rock-reservoir combination (Shi et al., 2015), which is the target layer in this study.

The reservoirs in this area have low permeabilities and abnormal formation pressures, with a pressure coefficient ranging from 1.20 to 1.50. The overpressure enhances the hydrocarbon migration and accumulation, and overcomes the effect of low permeability (Shi et al., 2015). The target layer has high oil saturation and low movable water/light oil quality. The porosity lies between 4% and 12%, and there are small areas with 15%. The average value is 8.5%, and the permeability ranges from 0.01 to 0.5 mD. The lithology is dominated by tight siltstones with high clay content. The thickness of the target layer is 70–110 m, the pore pressure range is 22–32 MPa and the temperature is around 80 °C (Ma et al., 2019).

The SEM of a tight-oil rock sample at different magnifications is shown in Fig. 2. The results of the image analysis showed that the reservoir storage space mainly includes the intergranular pores, dissolved pores and cracks, and the pore size lies between 5 and 100 μm. The pore structure has mainly small pores and throats, so that the permeability is low and the fluid flow is limited. However, secondary pores and cracks may contribute to the flow. The minerals mainly include quartz, feldspar, clay, and the small amounts of dolomite and calcite. The feldspar is plagioclase and potassium feldspar, and the clay mineral is illite.

2.2. Laboratory experiments

Twelve cores were collected from the target layer at the depth about 2.2 km, and the ultrasonic experiments were performed on the samples under reservoir conditions. The diameter is 25 mm and the lengths are between 50 mm and 56 mm. Standard materials (aluminum) with the same size and shape were also processed. The physical characteristics of the samples are given in Table 1. Under in-situ conditions (temperature 80 °C, pore pressure 25 MPa, and confining pressure 50 MPa), the ultrasonic experiments were performed on the water, gas (nitrogen), and oil (kerosene) saturated samples. The wave velocities were measured with the ultrasonic-pulse method at a frequency of 1 MHz.

The full-gas sample is dried by using an oven, sealed with a rubber sleeve, under a 50 MPa confining pressure, with the given pore pressure. The fluid in the vessel was then heated to 80 °C, and the P- and S-wave waveforms were measured. The sample was then saturated fully with oil and water, and as above, the waveform was recorded to obtain the wave velocity.

The P- and S-wave velocities vary with porosity and clay content (Fig. 3), where the velocities decrease with increasing clay content and

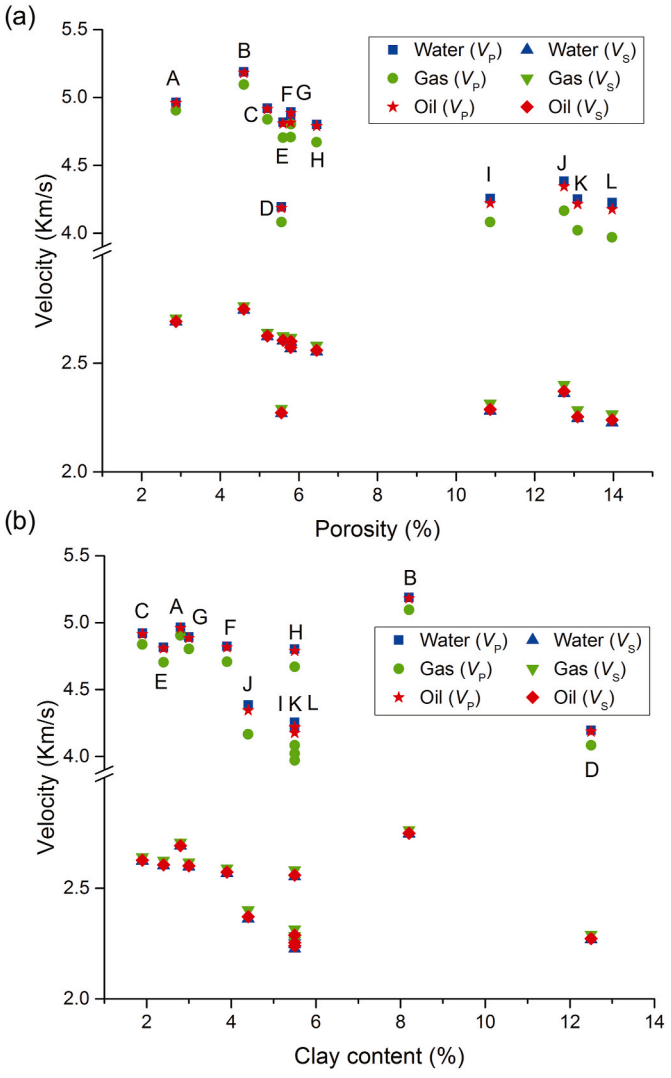

Fig. 3. The crossplots of P- and S-wave velocities versus porosity (a) and clay content (b).

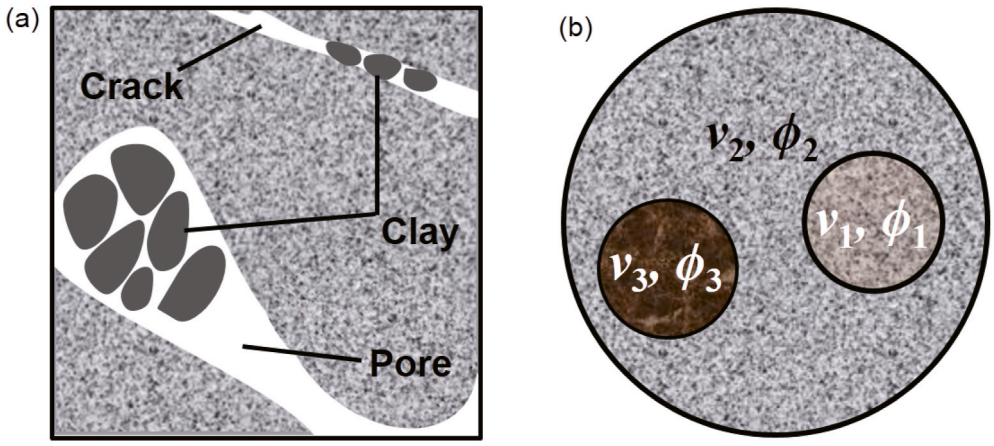

Fig. 4. Microstructure of a tight-oil rock (a) and a triple-porosity model (b). The quantities represent absolute porosity and volume ratio of host frame (φ_2 and v_2), crack (φ_1 and v_1) and clay (φ_3 and v_3) inclusions, where $\varphi_1 + \varphi_2 + \varphi_3$ is the overall porosity and $v_1 + v_2 + v_3 = 1$.

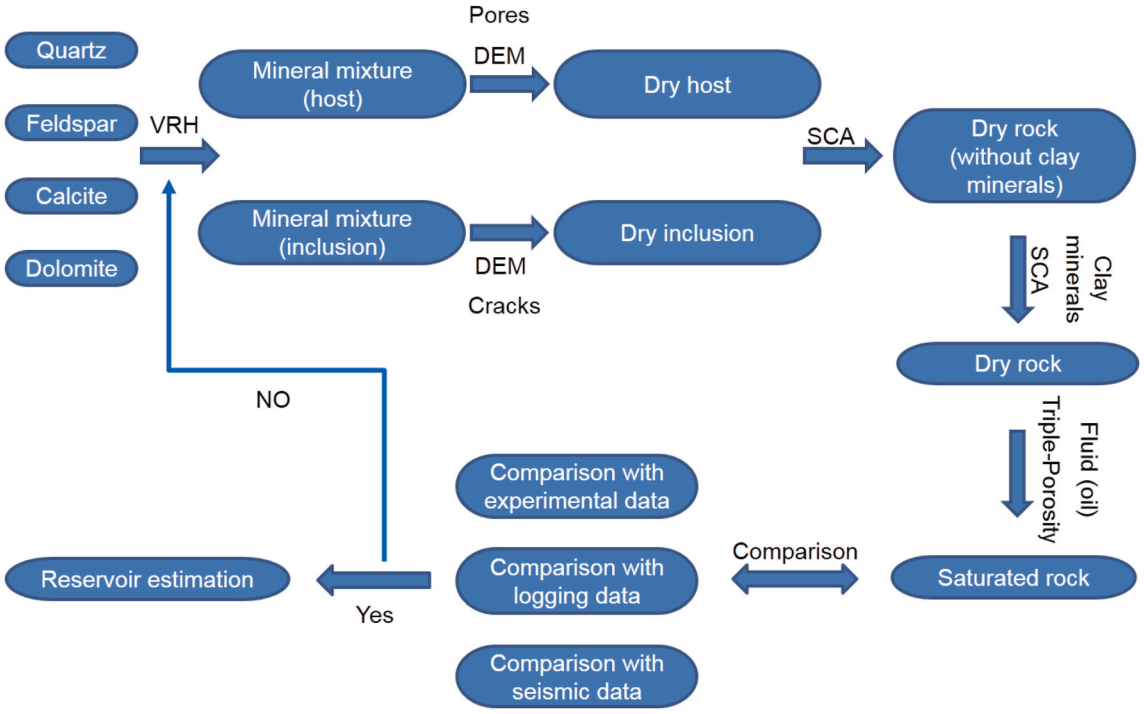

Fig. 5. Workflow of the modeling and reservoir estimation.

porosity. The S-wave velocity is almost the same for the different fluids. On the other hand, the P-wave velocities for the full-oil and full-water samples are similar and higher than that of the full-gas samples, but start to differ as porosity increases (Fig. 3a). Sample D shows lower values, because it comprises a high clay content. The trend of sample B differs from the other samples (Fig. 3b), in which the velocities being relatively high, likely caused by the low porosity.

3. Rock-physics model

The tight-oil rock pore system is complex, with equant pores and cracks, and a high clay content. Ba et al. (2016) regarded the clay minerals in the pores as inclusions, and obtained the wave properties of these rocks by using a double-porosity model, including velocity dispersion. The rock can be considered as a composite made of three homogeneous frames, related to intergranular pores, clay minerals and cracks (Fig. 4a). Here, a triple-porosity model was considered (Fig. 4b).

The workflow for the modeling and prediction procedures is shown in Fig. 5. In the first step, based on the SEM observations, the mineral composition was established as quartz, feldspar, clay, calcite and dolomite, and their bulk and shear moduli are 37/44 GPa, 37.5/15 GPa, 21/7 GPa, 76.8/32 GPa and 94.9/45 GPa, respectively. Minerals were mixed and the modulus of the mixture (excluding clay minerals) was estimated with the Voigt-Reuss-Hill equation (VRH, Voigt, 1910; Reuss, 1929; Hill, 1952).

The stiff pores and cracks are spherical and oblate, with aspect ratios

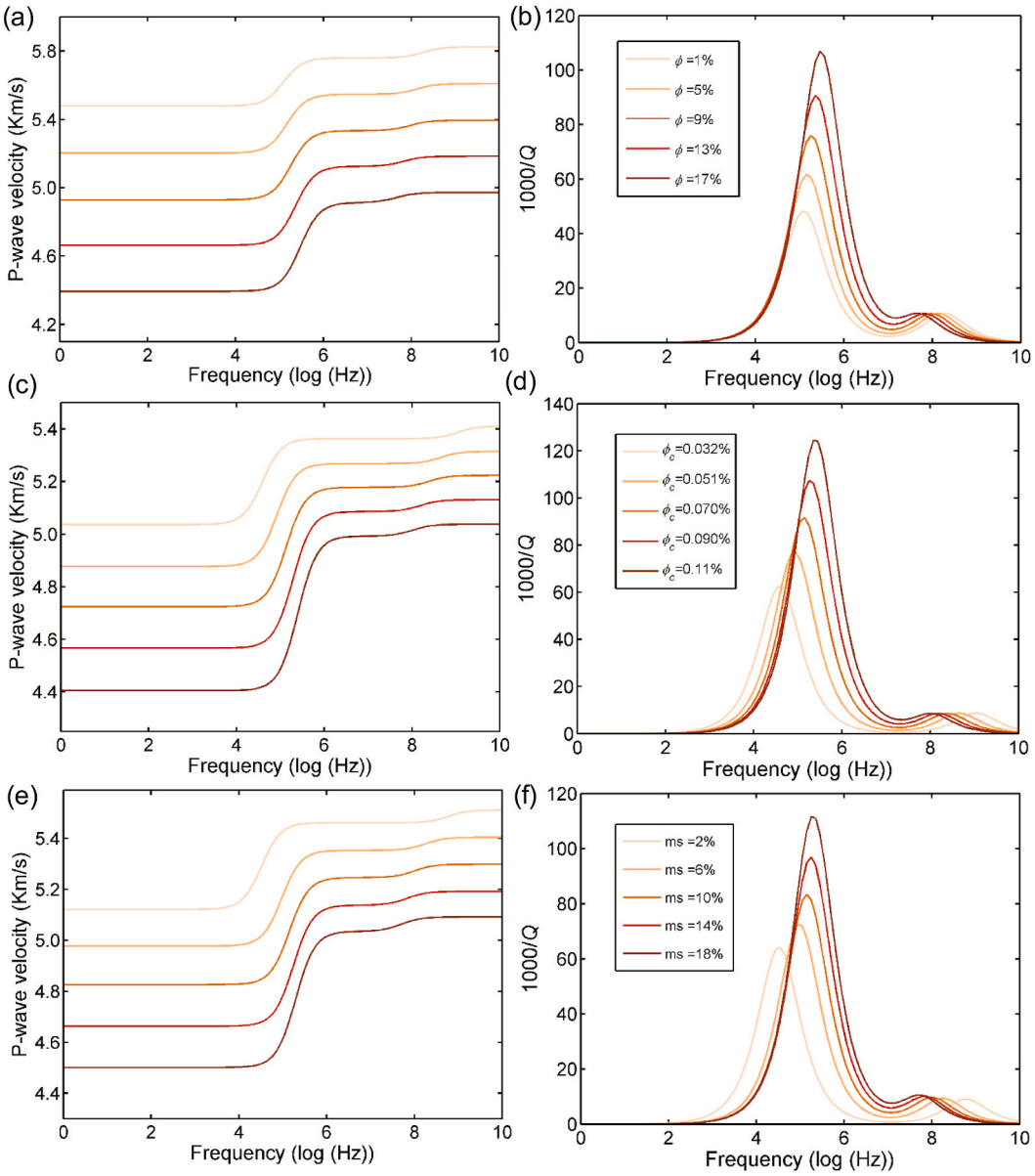

Fig. 6. The relationship of velocity dispersion and attenuation of the P wave with frequency at different values of "total" porosity (a–b), crack porosity (c–d), and clay content (e–f), shown in ms.

of 1 and 0.0003, respectively. The differential-effective-medium (DEM) theory (Berryman, 1992) was used to add pores and cracks into the host and inclusion mineral mixture and obtain the properties of the dry host and inclusions. Then, the self-consistent approximation (SCA) model (Berryman, 1980) was used to obtain the properties of the dry rock without and with the clay inclusions, and finally the triple-porosity model to compute the properties of the saturated rock.

More specifically, Berryman (1980) proposed the SCA equations to compute the bulk (M^*_{SC}) and shear (G^*_{SC}) moduli,

$$\sum c_i\left(M_i - M^*_{SC}\right)Q^{*i} = 0, \tag{1a}$$

$$\sum c_i\left(G_i - G^*_{SC}\right)P^{*i} = 0, \tag{1b}$$

where P^{*i} and Q^{*i} (Berryman, 1980, p. 3) are the geometrical factors of the ith component, M_i and G_i are bulk and shear moduli, and c_i is corresponding volume fraction for each component.

Berryman (1992) proposed the DEM equations for the elastic moduli (M^*, G^*),

$$(1-y)\frac{\mathrm{d}}{\mathrm{d}y}[M^*(y)] = (M_2 - M^*)Q^{(*2)}(y), \tag{2a}$$

$$(1-y)\frac{\mathrm{d}}{\mathrm{d}y}[G^*(y)] = (G_2 - G^*)P^{(*2)}(y), \tag{2b}$$

with initial conditions $M^*(0) = M_1$, $G^*(0) = G_1$, where M_1 and G_1 are the bulk and shear moduli of the host material, y is the content of phase 2, and M_2 and G_2 are the corresponding moduli. P and Q are the as above.

The Batzle and Wang (1992) equations were used to estimate the density and bulk modulus of the fluid. The triple-porosity medium equation was used for the fluid substitution to account for the effects of the fluid in cracks and pores on the wave velocities and attenuation. On the basis of the Biot-Rayleigh theory (Ba et al., 2011), the dynamic equations of the elastic wave propagation were established by incorporating the local fluid flow interaction into the dissipated energy, potential energy, and kinetic energy (Zhang et al., 2017):

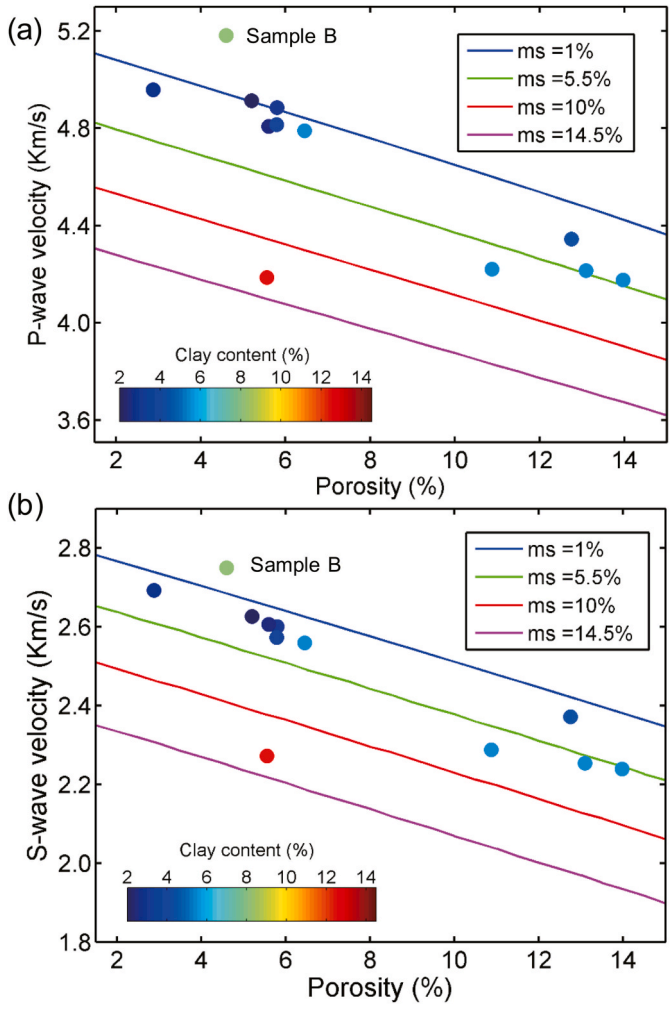

Fig. 7. P- (a) and S- (b) wave velocities versus porosity at different clay contents.

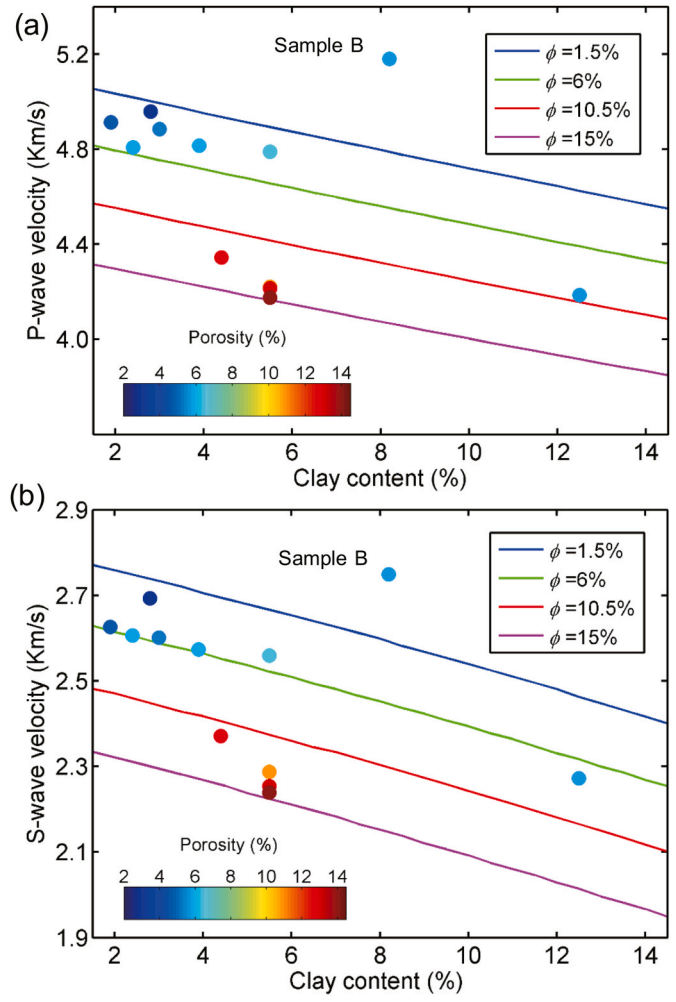

Fig. 8. P- (a) and S- (b) wave velocities versus clay content at different porosities.

$$N\nabla^2\mathbf{w}+(A+N)\nabla o+Q_1\nabla(\lambda_1+\varphi_2\delta_{12})+Q_2\nabla(\lambda-\varphi_1\delta_{12}+\varphi_3\delta_{23})+Q_3\nabla(\lambda_3-\varphi_2\delta_{23})$$
$$=a_1\left(\dot{\mathbf{w}}-\dot{\mathbf{W}}^{(1)}\right)+a_2\left(\dot{\mathbf{w}}-\dot{\mathbf{W}}^{(2)}\right)+a_3\left(\dot{\mathbf{w}}-\dot{\mathbf{W}}^{(3)}\right)+\rho_{00}\ddot{\mathbf{w}}+\rho_{01}\ddot{\mathbf{W}}^{(1)}+\rho_{02}\ddot{\mathbf{W}}^{(2)}+\rho_{03}\ddot{\mathbf{W}}^{(3)}, \tag{3a}$$

$$Q_1\nabla o+R_1\nabla(\lambda_1+\varphi_2\delta_{12})=-a_1\left(\dot{\mathbf{w}}-\dot{\mathbf{W}}^{(1)}\right)+\rho_{01}\ddot{\mathbf{w}}+\rho_{11}\ddot{\mathbf{W}}^{(1)}, \tag{3b}$$

$$Q_2\nabla o+R_2\nabla(\lambda_2-\varphi_1\delta_{12}+\varphi_3\delta_{23})=-a_2\left(\dot{\mathbf{w}}-\dot{\mathbf{W}}^{(2)}\right)+\rho_{02}\ddot{\mathbf{w}}+\rho_{22}\ddot{\mathbf{W}}^{(2)}, \tag{3c}$$

$$Q_3\nabla o+R_3\nabla(\lambda_3-\varphi_2\delta_{23})=-a_3\left(\dot{\mathbf{w}}-\dot{\mathbf{W}}^{(3)}\right)+\rho_{03}\ddot{\mathbf{w}}+\rho_{33}\ddot{\mathbf{W}}^{(3)}, \tag{3d}$$

$$\frac{1}{3}\rho_f\ddot{\delta}_{12}\varphi_1\varphi_2^2r_{12}^2\left(\frac{\varphi_{10}}{\varphi_{20}}+\frac{1}{5}\right)+\frac{1}{3}\left(\frac{\eta}{\kappa_2}+\frac{\eta}{5\kappa_1}\right)\dot{\delta}_{12}\varphi_{10}\varphi_1\varphi_2^2r_{12}^2$$
$$=\varphi_2(Q_1o+R_1(\lambda_1+\varphi_2\delta_{12}))-\varphi_1(Q_2o+R_2(\lambda_2-\varphi_1\delta_{12}+\varphi_3\delta_{23})), \tag{3e}$$

$$\frac{1}{3}\rho_f\ddot{\delta}_{23}\varphi_3\varphi_2^2r_{23}^2\left(\frac{\varphi_{30}}{\varphi_{20}}+\frac{1}{5}\right)+\frac{1}{3}\left(\frac{\eta}{\kappa_2}+\frac{\eta}{5\kappa_3}\right)\dot{\delta}_{23}\varphi_{30}\varphi_3\varphi_2^2r_{23}^2$$
$$=\varphi_3(Q_2o+R_2(\lambda_2-\varphi_1\delta_{12}+\varphi_3\delta_{23}))-\varphi_2(Q_3o+R_3(\lambda_3-\varphi_2\delta_{23})), \tag{3f}$$

where $\mathbf{w}$ denotes the solid displacement vector, and the displacement vectors of the cracks/pores, clay and pore fluid are $\dot{\mathbf{W}}^{(1)}$, $\dot{\mathbf{W}}^{(2)}$ and $\dot{\mathbf{W}}^{(3)}$, respectively; o, λ_1, λ_2 and λ_3 are the corresponding divergences. The stiffness coefficients A, N, Q_1, Q_2, Q_3, R_1, R_2 and R_3, the density ρ_{00}, ρ_{01}, ρ_{02}, ρ_{03}, ρ_{11}, ρ_{22} and ρ_{33}, and the dissipation coefficients a_1, a_2 and a_3 depend on the rock properties. The scalars δ_{12} and δ_{23} are the variations in fluid content between pores and cracks, and between clay minerals and pores, respectively. The quantities κ_1, κ_2 and κ_3 are the permeabilities of the crack, host and clay frames, respectively; r_{12} and

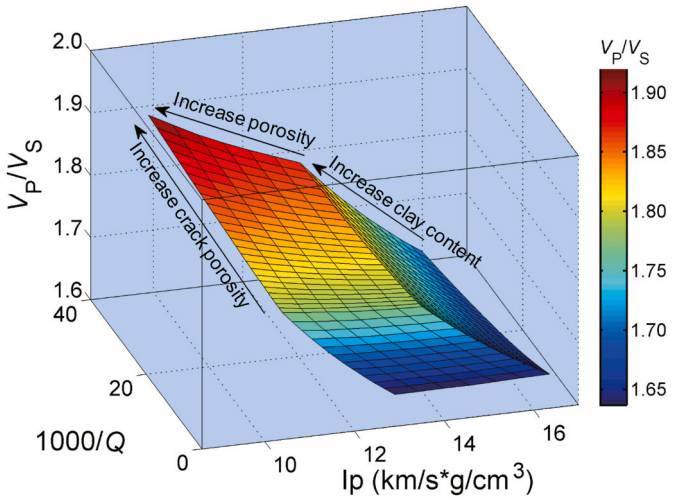

Fig. 9. 3D RPT at 1 MHz.

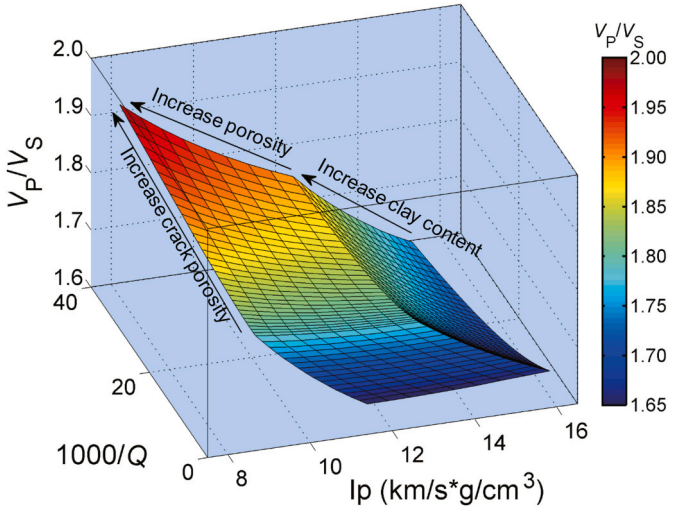

Fig. 10. 3D RPT at 10 KHz.

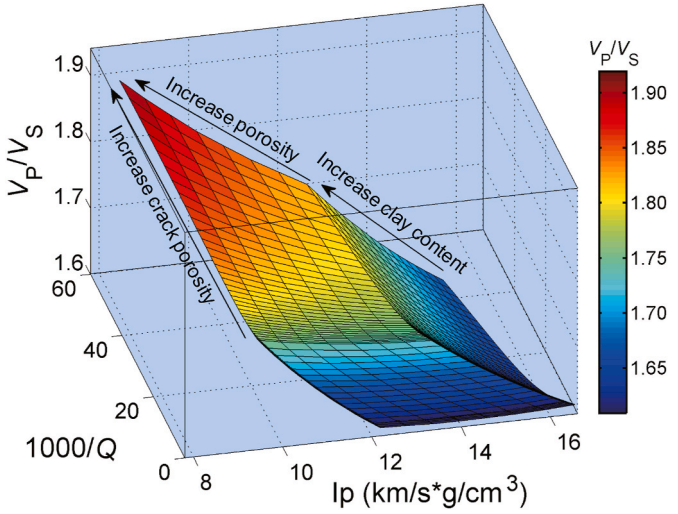

Fig. 11. 3D RPT at 35 Hz.

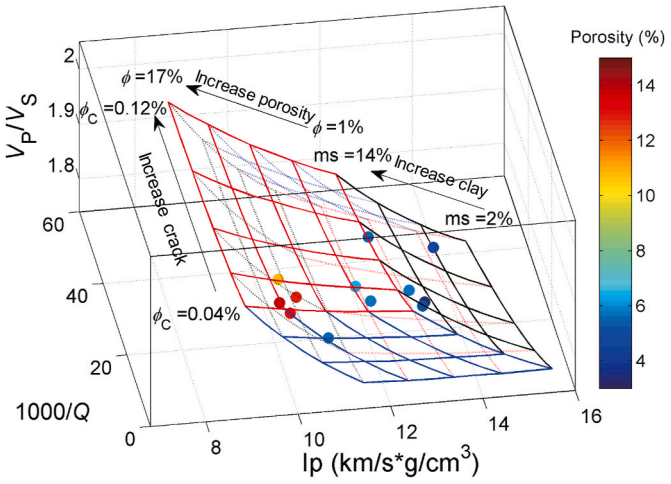

Fig. 12. 3D RPT and sample data, in which the color bar represents porosity. (For interpretation of the references to color in this figure legend, the reader is referred to the Web version of this article.)

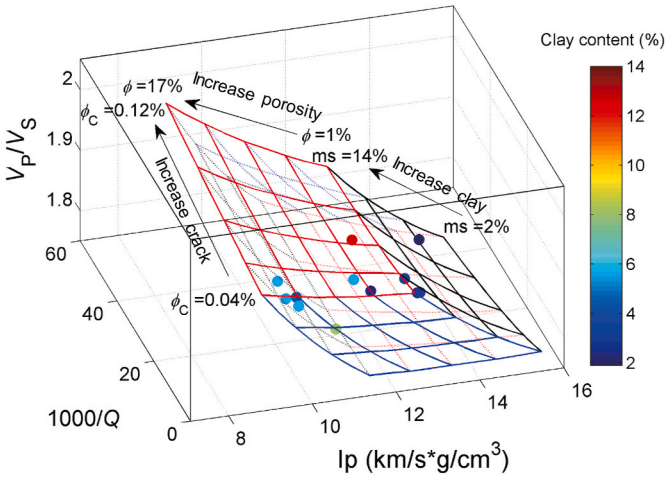

Fig. 13. 3D RPT and sample data, in which the color bar represents clay content. (For interpretation of the references to color in this figure legend, the reader is referred to the Web version of this article.)

r_{23} are the radii of the cracks and clay inclusions, respectively, η is viscosity, and ρ_f is the fluid density.

The complex wave number k can be computed by substituting a time harmonic kernel into equations (3a)-(3f) (see Appendix A), then the equation of P-wave velocity will be obtained as (Carcione, 2014),

$$V = \frac{1}{\mathrm{Re}(v^{-1})}, \tag{4a}$$

and attenuation,

$$\frac{1}{Q} = \frac{\mathrm{Im}(v^2)}{\mathrm{Re}(v^2)}, \tag{4b}$$

where the complex velocity v is obtained by dividing the angular frequency ω by k.

3.1. Wave properties

We simulated the effects of pore shape and crack size by considering different aspect ratios and inclusion radii, respectively. The model properties are as the following. Minerals proportion: quartz 43.6%,

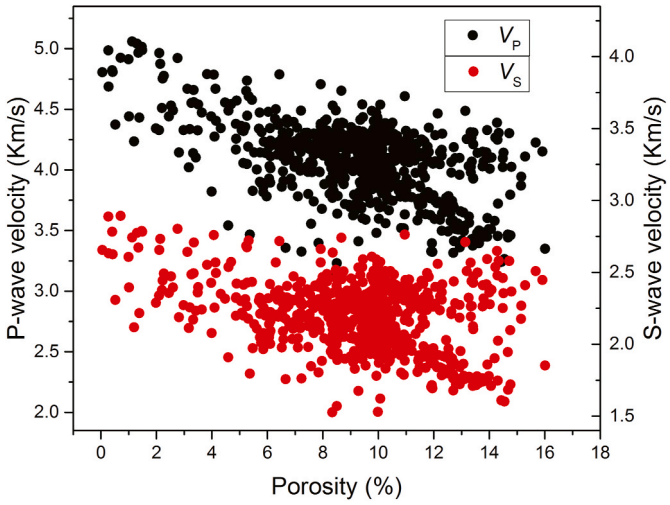

Fig. 14. Sonic velocities at well B versus porosity.

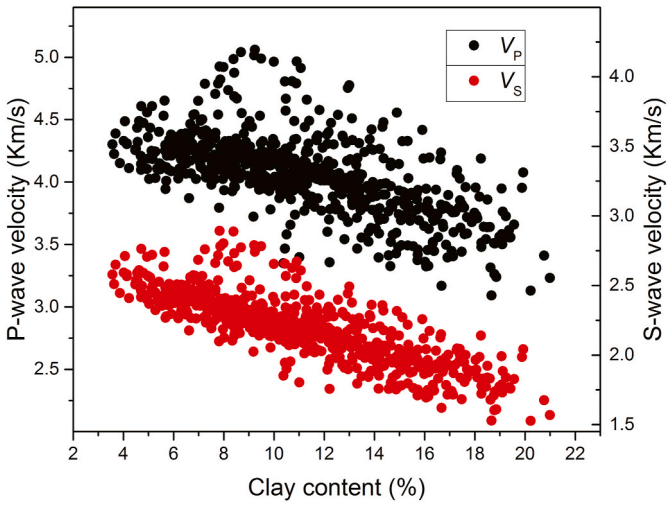

Fig. 15. Sonic velocities at well B versus clay content.

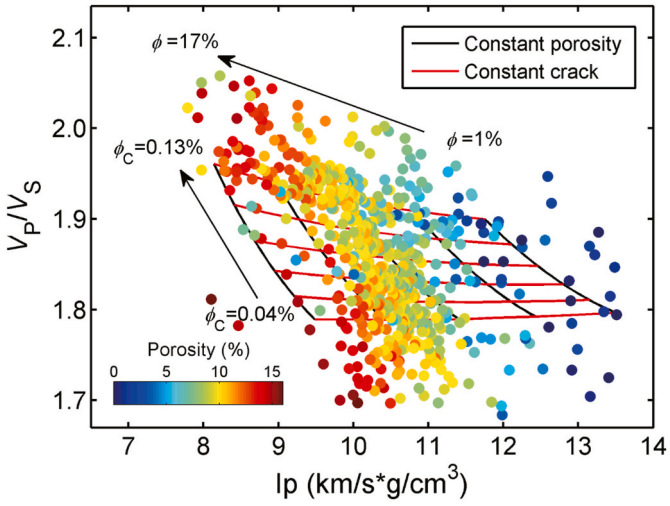

Fig. 16. 2D RPT at 10 KHz and log data, in which the color bar shows porosity. (For interpretation of the references to color in this figure legend, the reader is referred to the Web version of this article.)

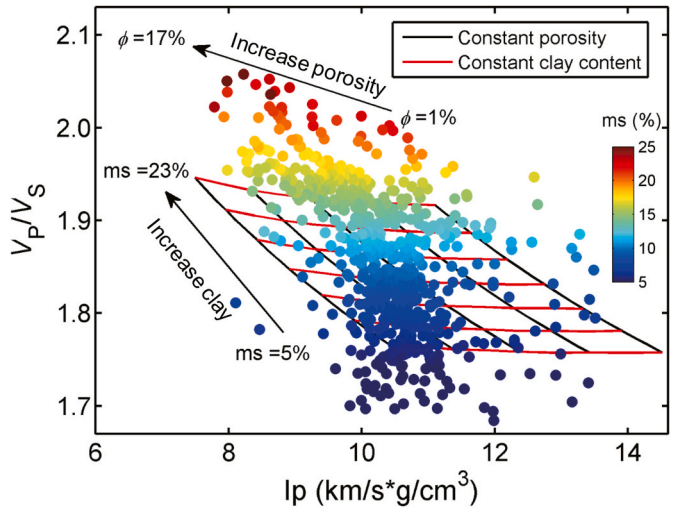

Fig. 17. 2D RPT at 10 KHz and log data, in which the color bar represents clay content. (For interpretation of the references to color in this figure legend, the reader is referred to the Web version of this article.)

feldspar 37.5%, calcite 4.6%, dolomite 2.3%, and clay mineral 12%; the aspect ratio of pores and cracks are 1 and 0.0003, respectively; the radius of crack and clay inclusions is 50 μm. The properties of oil are: bulk moduli 1.27 GPa; density 0.79 g/cm^3; viscosity 0.0021 Pa s. The VRH average equations were used to compute the modulus of the mineral mixture. The elastic moduli of the inclusions and rock frames were calculated by using the DEM and SCA models. By setting an oil-saturated condition, the influence of the clay content, as well as total and crack porosities, on the P-wave attributes were first analyzed.

The P-wave attributes vary with frequency at different reservoir properties (Fig. 6). In Figs. 6a and 6b, the crack porosity and clay content were set to 0.04% and 12%, respectively, and the total porosity varied as: 1%, 5%, 9%, 13% and 17%. In Figs. 6c and 6d, the porosity and clay content were set at 8% and 12%, respectively, and the crack porosity varied as: 0.032%, 0.051%, 0.07%, 0.09%, and 0.11%. Subsequently, in Figs. 6e and 6f, the total porosity and crack porosity were set at 8% and 0.04%, respectively, and the clay content varied as: 2%, 6%, 10%, 14% and 18%. Dispersion and attenuation increase with total and crack porosities as well as clay content, and two relaxation peaks were observed.

3.2. Comparison of the model-derived results and experimental values

The frequency is 1 MHz, and the crack porosity is 0.08%. The P- and S-wave velocities vary with porosity at different clay contents compared with the experimental values (Fig. 7). The agreement is good except for sample B. The relation between velocities and the clay content at different porosities is shown in Fig. 8. Except for sample B, the results agree well with the experimental values.

3.3. 3D rock-physics templates

The phase-velocity ratio, acoustic impedance and P-wave attenuation were set as the coordinate axes. By adjusting the clay content, total and crack porosities, a 3D rock-physics-template (RPT) was obtained. Fig. 9 shows the 3D RPT at 1 MHz, where the color scale is V_P/V_S. The attenuation and V_P/V_S increase with increasing reservoir properties, while the impedance decreases.

If the inclusion radius varies from 1 to 50 mm, the attenuation peaks at the sonic and seismic frequencies, respectively. The effects at 10 KHz and 35 Hz are shown in Figs. 10 and 11, which correspond to the sonic and seismic frequency bands, respectively. They are similar to the template at 1 MHz, except that the attenuation is stronger, and the seismic attributes have the same trend for the three studied reservoir

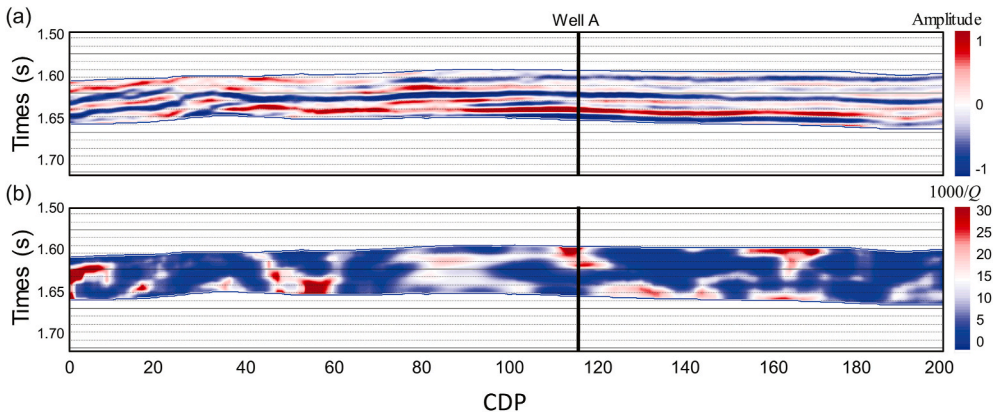

Fig. 18. Seismic amplitude (a) and Q value (b) of line 1.

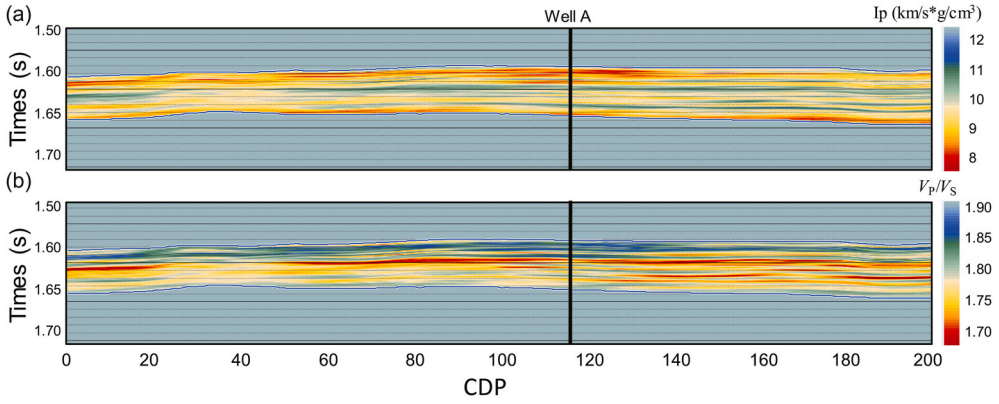

Fig. 19. Acoustic impedance (a) and phase-velocity ratio (b) of line 1.

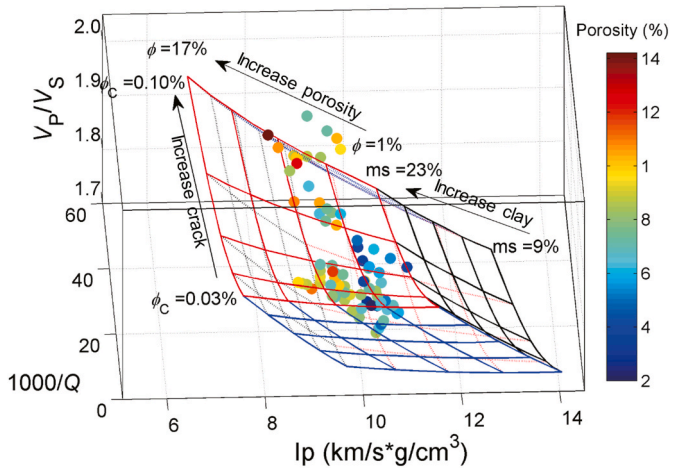

Fig. 20. 3D RPT and actual data, in which the color bar represents porosity. (For interpretation of the references to color in this figure legend, the reader is referred to the Web version of this article.)

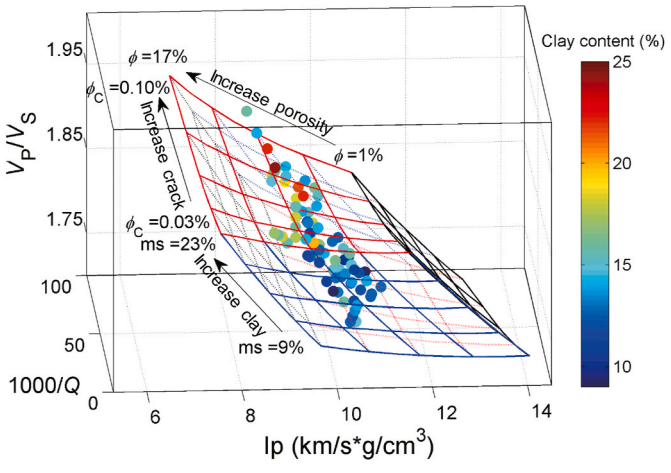

Fig. 21. 3D RPT and actual data, in which the color bar indicates clay content. (For interpretation of the references to color in this figure legend, the reader is referred to the Web version of this article.)

properties.

4. Multi-scale calibration of the 3D RPTs

4.1. Calibration at ultrasonic frequencies

Calibration is required for the templates, mainly including laboratory, well-log and seismic data. Fig. 12 compares the experimental data (circles) to the ultrasonic RPT, in which the black, blue and red curves indicate constant total porosity, crack porosity and clay content, respectively. The quality factor Q was estimated by using an aluminum block as a reference material (see equation A-4). The color bar of the circles is porosity, which agrees well with the template results. As inferred from the data and template, there is the same trend between V_P/V_S, impedance, attenuation and porosity. Fig. 13 shows the template and sample data, in which the color bar indicates clay content. The clay

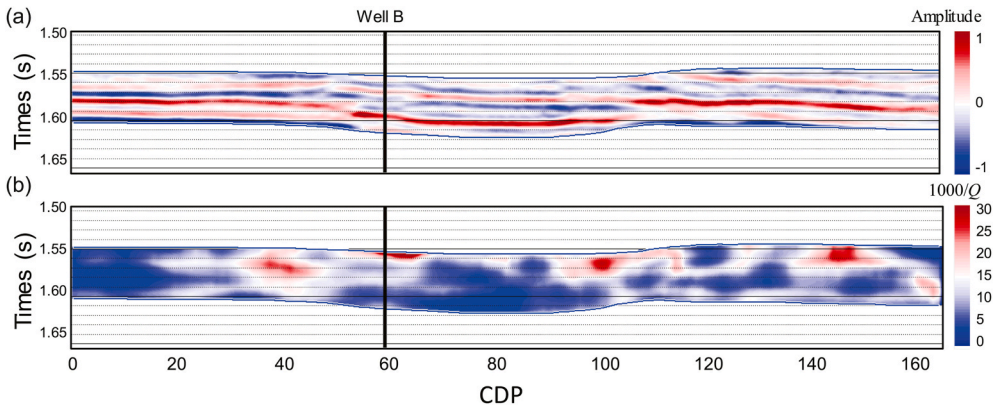

Fig. 22. Seismic amplitude (a) and Q value (b) of line 2.

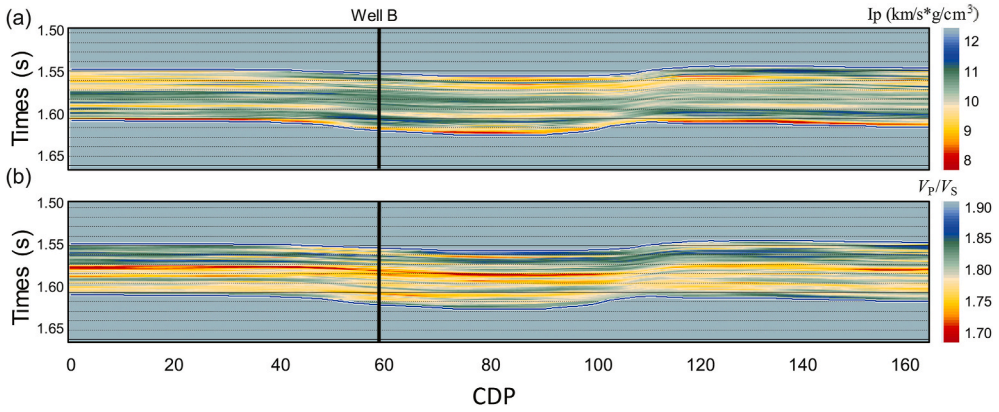

Fig. 23. Acoustic impedance (a) and phase-velocity ratio (b) of line 2.

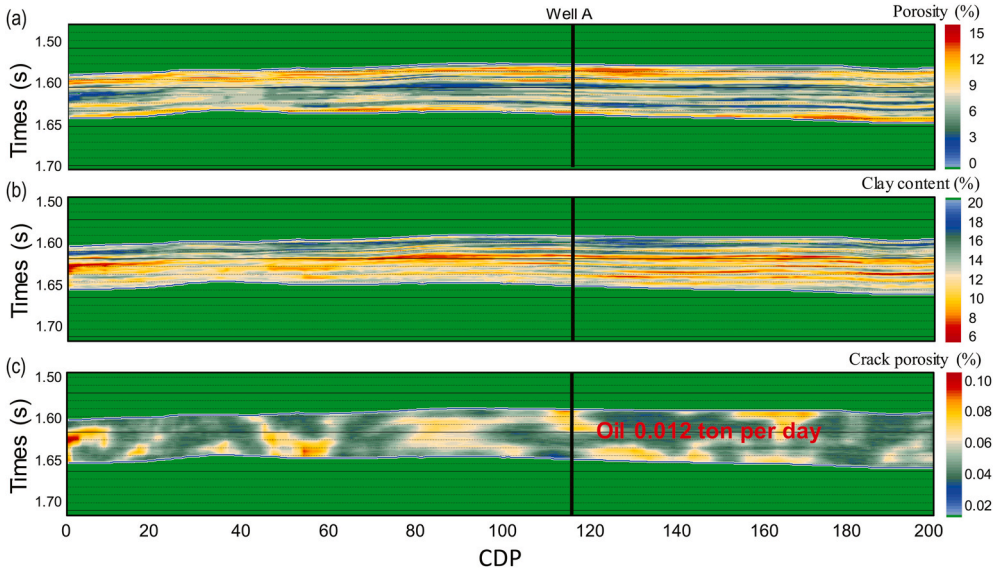

Fig. 24. Total porosity (a), clay content (b) and crack porosity (c) of line 1.

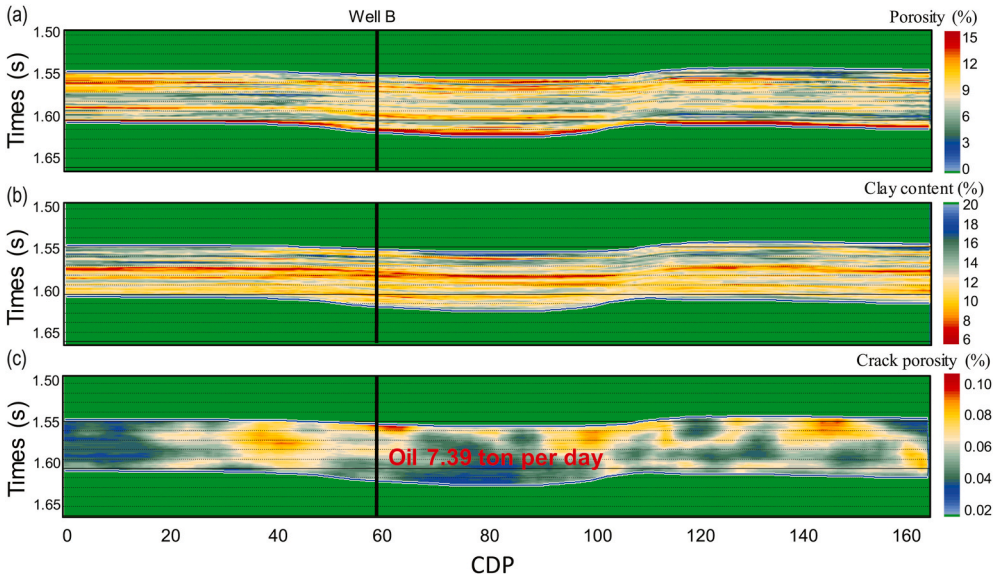

Fig. 25. Total porosity (a), clay content (b) and crack porosity (c) of line 2.

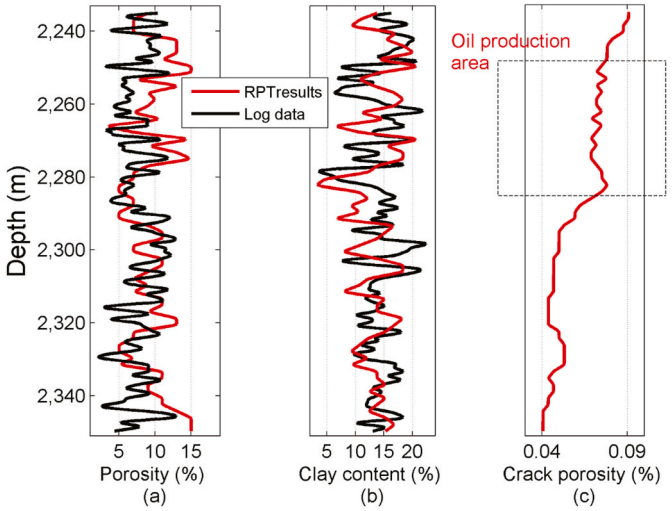

Fig. 26. Comparison of the total porosity (a), clay content (b) and crack porosity (c) predictions with the log data (Well A) and oil production report.

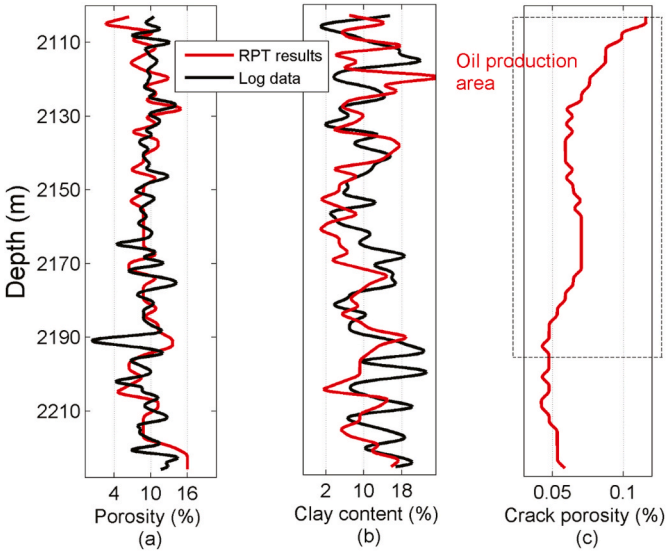

Fig. 27. Comparison of the total porosity (a), clay content (b) and crack porosity (c) predictions with the log data (Well B) and oil production report.

content of the samples is lower than that of the template. Two trends are similar as a function of clay content.

4.2. Calibration at sonic frequencies

The sonic velocities versus porosity at well B are given in Fig. 14. The velocities decrease when porosity increases, which lies in the range [4, 15] %. The clay content was calculated by using the Gamma-ray log, as indicated in Appendix A. Fig. 15 shows the velocities versus clay content, whose range is [5, 20] %, and, as expected, the velocities decrease with increasing clay content. There is a defined linear relation between clay content and S-wave velocity.

Well B data was used to calibrate the template at 10^4 Hz. Due to the lack of attenuation at this frequency, the V_P/V_S - acoustic impedance template was used for comparison with the well data. Figs. 16 and 17 show the data of well B compared to the RPT. The color bars indicate the porosity and clay content (circles), respectively. The behavior of the theory is consistent with the data, since the impedance decreases with increasing porosity, and V_P/V_S gradually increases with enhancing clay content.

Table 2
Log and prediction average values for two studied wells.

		Logging data	RPT results
Well A	Porosity (%)	7.68	8.46
	Clay content (%)	14.13	13.49
	Crack porosity (%)		0.0606
Well B	Porosity (%)	9.27	9.60
	Clay content (%)	10.75	9.61
	Crack porosity (%)		0.0688

4.3. Estimation of attenuation

The generalized S transform is used for the time-frequency analysis, based on the seismic data, and an improved frequency-shift method (see

equation A-5) is implemented to estimate seismic Q by assuming a Ricker wavelet (Pang et al., 2019, 2020). Fig. 18 shows a 2D seismic survey (line 1 crossing well A), the seismic amplitude and Q value of the reservoirs, and the line indicates the position of the well. In Fig. 18b, the blue and red areas represent the weak and strong attenuation, respectively. The result shows that there is an abnormal attenuation in well A.

4.4. Calibration at seismic frequencies

The Ip and V_P/V_S were computed with three-dimensional inversion (Fig. 19). These attributes along with the seismic Q in well A were used to calibrate the 3D template at 35 Hz. Figs. 20 and 21 show the comparisons between the corresponding templates and the seismic data (circles). The color bars indicate porosity and clay content, respectively, which agree well with the templates. Low porosity and high clay content are observed from the templates and seismic data. By using the seismic data to obtain the three attributes (i.e. Ip, V_P/V_S and seismic Q), the best reservoir areas can be quantitatively predicted by superposing the template and data.

5. Prediction

Seismic Q (Fig. 22), V_P/V_S and Ip (Fig. 23) were also extracted for line 2 in well B. The reservoir porosities and clay content were quantitatively estimated for the two survey lines by overlapping these seismic attributes onto the RPT. Figs. 24 and 25 show the 2D estimation profiles of the total porosity, clay content and crack porosity of the two survey lines. The results show that the clay content, total porosity and crack porosity of the reservoirs range in 5–20%, 3–15%, and 0.02–0.12%, respectively. Compared to well A, well B shows higher total (equant) and crack porosities, and lower clay content. Thus, the area where well B is located has a better connectivity and higher oil storage potential. The reports indicate that the oil production from wells A and B are 0.012 and 7.39 tons per day, respectively, which is in good agreement with the estimations.

Figs. 26 and 27 compare the predictions in wells A and B with the actual production reports and log data, respectively. The porosity and clay content curves of the two wells are similar to the predictions, and the oil producing sections are distributed in areas with high crack porosity.

The storage conditions and actual results of two wells were compared by averaging the log curves and predictions (Table 2). Compared to the log data, the predictions at two wells represent higher porosity and lower clay content. Moreover, the total and crack porosities in well B are higher than well A, while the clay content is lower. Thus, well B has better reservoir properties and higher storage capacity, which is consistent with the actual oil production results.

6. Conclusions

Scanning electron microscope (SEM) and ultrasonic experiments were performed on a suite of rock samples from the target formation to establish the microstructural characteristics of the tight-oil reservoirs rocks and to investigate the effects of porosity and clay content on the wave velocities. The complex micro-structural features of these rocks were simulated with the self-consistent and differential-effective-medium (DEM) theories, and a triple-porosity model to obtain the fluid-saturated properties. The effects of round pores, cracks and clay minerals on the dispersion and attenuation of P-wave velocity were analyzed. Then, the wave velocities with clay content and porosity were compared to the experimental data. The model made it possible to build a multi-scale 3D rock-physics template. Ultrasonic waveforms, log and seismic data were used to estimate the attenuation of the rock samples, the clay content and the seismic Q. The templates are calibrated and then used to estimate reservoir properties.

Two 2D seismic lines crossing two wells were considered. The 3D template was used to predict the reservoir properties. The obtained results were compared to the log data and production reports, which represented a good agreement. One of the studied wells shows higher total (equant) and crack porosities and lower clay content, which agrees with the production reports.

Credit author statement

Mengqiang Pang: Methodology, Software, Coding, Writing – original draft preparation. Jing Ba: Conceptualization, Supervision, Writing – original draft preparation, Funding acquisition. José M.Carcione: Conceptualization, Supervision, Proofreading. Lin Zhang: Validation, Modeling. Rupeng Ma: Formal analysis, Modeling. Yijun Wei: Modeling, Field data application.

Declaration of competing interest

The authors declare that they have no known competing financial interests or personal relationships that could have appeared to influence the work reported in this paper.

Acknowledgements

The authors appreciate the helpful comments from the editor, Rouhi Farajzadeh, and reviewers, and this work is supported the Science and Technology Innovation Project for Oversea Scholar of Nanjing, the National Natural Science Foundation of China (grant no. 41974123) and the Jiangsu Innovation and Entrepreneurship Plan and the Jiangsu Province Science Fund for Distinguished Young Scholars (grant no. BK20200021).

Appendix B. Supplementary data

Supplementary data to this article can be found online at https://doi.org/10.1016/j.petrol.2021.108476.

Appendix A

Dispersion equations

The k is obtained by substituting a time harmonic kernel $e^{i(\omega t - k\cdot\mathbf{x})}$ into equations (3a)-(3f) as,

$$\begin{vmatrix} b_{11}k^2+c_{11} & b_{12}k^2+c_{12} & b_{13}k^2+c_{13} & b_{14}k^2+c_{14} \\ b_{21}k^2+c_{21} & b_{22}k^2+c_{22} & b_{23}k^2+c_{23} & b_{24}k^2+c_{24} \\ b_{31}k^2+c_{31} & b_{32}k^2+c_{32} & b_{33}k^2+c_{33} & b_{34}k^2+c_{34} \\ b_{41}k^2+c_{41} & b_{42}k^2+c_{42} & b_{43}k^2+c_{43} & b_{44}k^2+c_{44} \end{vmatrix} = 0, \tag{A-1}$$

and

$$\begin{aligned}
&b_{11} = A + 2N + (Q_1\varphi_2 - Q_2\varphi_1)M_0^{(12)} + (Q_2\varphi_3 - Q_3\varphi_2)M_0^{(23)},\\
&b_{21} = Q_1 + \varphi_2 R_1 M_0^{(12)}, b_{31} = Q_2 - R_2\left(\varphi_1 M_0^{(12)} - \varphi_3 M_0^{(23)}\right),\\
&b_{41} = Q_3 - \varphi_2 R_3 M_0^{(23)},\\
&b_{12} = Q_1 + (Q_1\varphi_2 - Q_2\varphi_1)M_1^{(12)} + (Q_2\varphi_3 - Q_3\varphi_2)M_1^{(23)},\\
&b_{22} = R_1 + \varphi_2 R_1 M_1^{(12)}, b_{32} = -R_2\left(\varphi_1 M_1^{(12)} - \varphi_3 M_1^{(23)}\right),\\
&b_{42} = -\varphi_2 R_3 M_1^{(23)},\\
&b_{13} = Q_2 + (Q_1\varphi_2 - Q_2\varphi_1)M_2^{(12)} + (Q_2\varphi_3 - Q_3\varphi_2)M_2^{(23)},\\
&b_{23} = \varphi_2 R_1 M_2^{(12)}, b_{33} = R_2\left(1 - \varphi_1 M_2^{(12)} + \varphi_3 M_2^{(23)}\right),\\
&b_{43} = -\varphi_2 R_3 M_2^{(23)},\\
&b_{14} = Q_3 + (Q_1\varphi_2 - Q_2\varphi_1)M_3^{(12)} + (Q_2\varphi_3 - Q_3\varphi_2)M_3^{(23)},\\
&b_{24} = \varphi_2 R_1 M_3^{(12)}, b_{34} = R_2\left(-\varphi_1 M_3^{(12)} + \varphi_3 M_3^{(23)}\right),\\
&b_{44} = R_3\left(1 - \varphi_2 M_3^{(23)}\right),\\
&c_{11} = -\rho_{00}\omega^2 + i\omega(a_1 + a_2 + a_3), c_{21} = -\rho_{01}\omega^2 - i\omega a_1,\\
&c_{31} = -\rho_{02}\omega^2 - i\omega a_2, c_{41} = -\rho_{03}\omega^2 - i\omega a_3,\\
&c_{12} = -\rho_{01}\omega^2 - i\omega a_1, c_{22} = -\rho_{11}\omega^2 + i\omega a_1,\\
&c_{32} = c_{34} = 0, c_{42} = c_{43} = 0,\\
&c_{13} = -\rho_{02}\omega^2 - i\omega a_2, c_{23} = c_{24} = 0, c_{33} = -\rho_{22}\omega^2 + i\omega a_2,\\
&c_{14} = -\rho_{03}\omega^2 - i\omega a_3, c_{44} = -\rho_{33}\omega^2 + i\omega a_3,
\end{aligned} \tag{A-2}$$

where

$$S_{12} = \frac{-\varphi_1\varphi_2^2 r_{12}^2\omega\left(\omega\rho_f(\varphi_{10}/\varphi_{20} + 1/5) + i(\eta/\kappa_2 + \eta/(5\kappa_1))\varphi_{10}\right)}{3} - \varphi_1^2 R_2 - \varphi_2^2 R_1,$$

$$S_{23} = \frac{-\varphi_3\varphi_2^2 r_{23}^2\omega\left(\omega\rho_f(\varphi_{30}/\varphi_{20} + 1/5) + i(\eta/\kappa_2 + \eta/(5\kappa_3))\varphi_{30}\right)}{3} - \varphi_2^2 R_3 - \varphi_3^2 R_2,$$

$$M_0^{(12)} = \frac{(Q_1\varphi_2 - Q_2\varphi_1)/S_{12} + \varphi_1\varphi_3 R_2(Q_2\varphi_3 - Q_3\varphi_2)/(S_{12}S_{23})}{1 + (\varphi_1\varphi_3 R_2)^2/(S_{12}S_{23})},$$

$$M_0^{(23)} = \left(-M_0^{(12)}\varphi_1\varphi_3 R_2 + Q_2\varphi_3 - Q_3\varphi_2\right)/S_{23},$$

$$M_1^{(12)} = \frac{\varphi_2 R_1/S_{12}}{1 + (\varphi_1\varphi_3 R_2)^2/(S_{12}S_{23})}, M_1^{(23)} = -M_1^{(12)}\varphi_1\varphi_3 R_2/S_{23},$$

$$M_2^{(12)} = \frac{-\varphi_1 R_2/S_{12} + \varphi_1\varphi_3^2 R_2^2/(S_{12}S_{23})}{1 + (\varphi_1\varphi_3 R_2)^2/(S_{12}S_{23})},$$

$$M_2^{(23)} = \left(-M_2^{(12)}\varphi_1\varphi_3 R_2 + \varphi_3 R_2\right)/S_{23},$$

$$M_3^{(12)} = \frac{-\varphi_1\varphi_2\varphi_3 R_2 R_3/(S_{12}S_{23})}{1 + (\varphi_1\varphi_3 R_2)^2/(S_{12}S_{23})},$$

$$M_3^{(23)} = \left(-M_3^{(12)}\varphi_1\varphi_3 R_2 - \varphi_2 R_3\right)/S_{23}. \tag{A-3}$$

Q estimation

The spectral-ratio method is (Toksöz et al., 1979; Ma and Ba, 2020),

$$\ln\left[\frac{A_1(f)}{A_2(f)}\right] = \ln\left[\frac{G_1(f)}{G_2(f)}\right] - \frac{\pi f x}{VQ}, \tag{A-4}$$

where $A_1(f)/A_2(f)$ is the spectra, x is the sample length, $G(f)$ is the geometrical factor, and V is the P-wave velocity. On the other hand, the seismic attenuation can be obtained from (Pang et al., 2020),

$$\frac{1}{Q} = \frac{16\left(f_{C0}^2 - f_{C1}^2\right)}{\sqrt{\pi^5} t f_{C0}^2 f_{C1}}, \tag{A-5}$$

where f_{c0}/f_{c1} is the centroid frequency of the signal before/after propagation, and t is the propagation time.

Clay-volume estimation

The Gamma-ray (Gr) log yields the clay content. The equations are (Li 2018),

$$I_{Gr} = (Gr - Gr_{\min})/(Gr_{\max} - Gr_{\min}), \tag{A-6}$$

$$Ms = \left(2^{\beta * I_{Gr}} - 1\right)/(2^{\beta} - 1) \tag{A-7}$$

where I_{Gr} is the mud-content index, Gr, $Gr_{\min}$ and $Gr_{\max}$ are the natural Gr values of the layer, sandstone and mudstone, respectively, Ms is the clay volume and β is the Hirsch index, which is related to the formation age (new: 3.7; old: 2). The target layer is the Mesozoic Cretaceous Upper System Qingshankou formation, which was formed during the first lake flooding period. The thickness of the continuous deposition reaches 550 m, and there is no older formation, so the target layer is considered to be a new stratum.

References

Andersen, C.F., Grosfeld, V., Wijngaarden, A.V., Haaland, A.N., 2009. Interactive interpretation of 4D prestack inversion data using rock physics templates, dual classifi cation, and real-time visualization. Lead. Edge 28 (8), 898–906.

Ba, J., Carcione, J.M., Nie, J., 2011. Biot-Rayleigh theory of wave propagation in double-porosity media. J. Geophys. Res. 116, B06202. https://doi.org/10.1029/2010JB008185.

Ba, J., Zhao, J.G., Carcione, J.M., Huang, X.X., 2016. Compressional wave dispersion due to rock matrix stiffening by clay squirt flow. Geophys. Res. Lett. 43, 6186–6195.

Ba, J., Ma, R., Carcione, J.M., Picotti, S., 2019. Ultrasonic wave attenuation dependence on saturation in tight oil siltstones. J. Petrol. Sci. Eng. 179, 1114–1122. https://doi.org/10.1016/j.petrol.2019.04.099.

Batzle, M.L., Wang, Z., 1992. Seismic properties of pore fluids. Geophysics 57, 1396–1408.

Benaafi, M., Hariri, M., Bertotti, G., Al-Shaibani, A., Abdullatif, O., Makkawi, M., 2019. Natural fracture system of the cambro-permian wajid group, wadi Al-dawasir, SW Saudi Arabia. J. Petrol. Sci. Eng. 175, 140–158.

Berryman, J.G., 1980. Long-wavelength propagation in composite elastic media. J. Acoust. Soc. Am. 68 (6), 1809–1831. https://doi.org/10.1121/1.385171.

Berryman, J.G., 1992. Single-scattering approximations for coefficients in Biot's equations of poroelasticity. Acoustical Society of America Journal 91 (2), 551–571.

Carcione, J.M., 2014. Wave fields in real media. In: Theory and Numerical Simulation of Wave Propagation in Anisotropic, Anelastic, Porous and Electromagnetic Media, third ed. Elsevier.

Carcione, J.M., Avseth, P., 2015. Rock-physics templates for clay-rich source rocks. Geophysics 80 (5), D481–D500. https://doi.org/10.1190/GEO2014-0510.1.

Carcione, J.M., Gurevich, B., Santos, J.E., Picotti, S., 2013. Angular and frequency dependent wave velocity and attenuation in fractured porous media. Pure Appl. Geophys. 170, 1673–1683.

Chapman, M., 2003. Frequency-dependent anisotropy due to meso-scale fractures in the presence of equant porosity. Geophys. Prospect. 51, 369–379.

Cheng, W., Ba, J., Fu, L., Lebedev, M., 2019. Wave-velocity dispersion and rock microstructure. J. Petrol. Sci. Eng. 183 org/10.1016/j.petrol.2019.106466.

Crampin, S., Bamford, D., 1977. Inversion of P-wave velocity anisotropy. Geophys. J. Int. 49 (1), 123–132.

Das, P.S., Chatterjee, R., Dasgupta, S., Das, R., Bakshi, D., Gupta, M., 2019. Quantification and spatial distribution of pore-filling materials through constrained rock physics template and fluid response modelling in Paleogene clastic reservoir from Cauvery basin, India. Geophys. Prospect. 67 (1), 150–166. https://doi.org/10.1111/1365-2478.12715.

Golikov, P., Avseth, P., Stovas, A., Bachrach, R., 2012. Rock physics interpretation of heterogeneous and anisotropic turbidite reservoirs. Geophys. Prospect. 61 (2), 448–457.

Gupta, S.D., Chatterjee, R., Farooqui, M.Y., 2012. Rock physics template (RPT) analysis of well logs and seismic data for lithology and fluid classification in Cambay Basin. Int. J. Earth Sci. 101 (5), 1407–1426. https://doi.org/10.1007/s00531-011-0736-1.

Gurevich, B., Brajanovski, M., Galvin, R.J., Muller, T.M., Toms-Stewart, J., 2009. P-wave dispersion and attenuation in fractured and porous reservoirs-poroelasticity approach. Geophys. Prospect. 57 (2), 225–237. https://doi.org/10.1111/j.1365-2478.2009.00785.x.

Hill, R., 1952. The elastic behaviour of a crystalline aggregate. Proc. Phys. Soc. 65 (5), 349–354. https://doi.org/10.1088/0370-1298/65/5/307.

Hu, J., Sun, R., Zhang, Y., 2020. Investigating the horizontal well performance under the combination of micro-fractures and dynamic capillary pressure in tight oil reservoirs. Fuel 269 org/10.1016/j.fuel.2020.117375.

Li, Z., 2018. Processing and Comprehensive Interpretation of Geophysical Well-Logging Data. Beijing Geological Publisher.

Li, D., Liu, Z., Zhang, G., Zheng, Z., Jia, J., Gao, X., Zan, X., 2017. Comparison and revelation of tight oil accumulation conditions, distribution characteristics and development status between China and U.S. Nat Gas Geosci 28, 1126–1138.

Li, C., Wang, H., Wang, L., Kang, Y., Hu, K., Zhu, Y., 2020. Characteristics of tight oil sandstone reservoirs: a case study from the upper triassic chang 7 member in zhenyuan area, Ordos basin, China. Arabian Journal of Geosciences 13, 78 org/10.1007/s12517-019-4964-1.

Liu, L., Tang, D., Wo, Y., Liu, L., Sun, W., Lu, H., Mbunkah, Q., 2019. Favorable area prediction of tight sandstone: a case study of the He8 formation in the Kangning area, Eastern Ordos Basin, China. J. Petrol. Sci. Eng. 175, 430–443 org/10.1016/j.petrol.2018.12.069.

Ma, R., Ba, J., 2020. Coda and intrinsic attenuations from ultrasonic measurements in tight siltstones. J. Geophys. Res. 125 (4) https://doi.org/10.1029/2019JB018825.

Ma, R., Ba, J., Carcione, J.M., Zhou, X., Li, F., 2019. Dispersion and attenuation of compressional waves in tight oil reservoirs: experiments and simulations. Appl. Geophys. 16 (1), 33–45. https://doi.org/10.1007/s11770-019-0748-3.

Nelson, R., 2001. Geologic Analysis of Naturally Fractured Reservoirs. Elsevier.

Nelson, P.H., 2009. Pore-throat sizes in sandstones, tight sandstones, and shales. AAPG Bull. 93, 329–340.

Nicolás-López, R., Valdiviezo-Mijangos, O.C., 2016. Rock physics templates for integrated analysis of shales considering their mineralogy, organic matter and pore fluids. J. Petrol. Sci. Eng. 137, 33–41.

Odegaard, E., Avseth, P.A., 2004. Well log and seismic data analysis using rock physics templates. First Break 22 (10), 37–43.

Pang, M., Ba, J., Carcione, J.M., Picotti, S., Zhou, J., Jiang, R., 2019. Estimation of porosity and fluid saturation in carbonates from rock-physics templates based on seismic Q. Geophysics 84 (6), M25–M36. https://doi.org/10.1190/geo2019-0031.1.

Pang, M., Ba, J., Fu, L., Carcione, J.M., Markus, U.I., Zhang, L., 2020. Estimation of microfracture porosity in deep carbonate reservoirs based on 3D rock-physics templates. Interpretation 8 (4), SP43–SP52. https://doi.org/10.1190/INT-2019-0258.1.

Reuss, A., 1929. Calculation of the flow limits of mixed crystals on the basis of the plasticity of monocrystals. Z. Angew. Math. 9, 49–58.

Sakhaee-Pour, A., Bryant, S.L., 2014. Effect of pore structure on the producibility of tight-gas sandstones. AAPG Bull. 98, 663–694.

Shi, L., Wang, Z., Zhang, G., Zhang, Y., Xing, E., 2015. Distribution and formation of tight oil in Qijia area, Songliao Basin, NE China. Petrol. Explor. Dev. 42 (1), 48–55.

Smith, T.M., Sayers, C.M., Sondergeld, C.H., 2009. Rock properties in low-porosity/low permeability sandstones. Lead. Edge 28 (1), 48–59.

Stroker, T., Harris, N., Elliott, W., Wampler, J., 2013. Diagenesis of a tight gas sand reservoir: upper cretaceous mesaverde group, piceance basin, Colorado. Mar. Petrol. Geol. 40, 48–68.

Sun, Y., Wu, Q., Wei, M., Bai, B., Ma, Y., 2014. Experimental study of friction reducer flows in microfracture. Fuel 131, 28–35.

Tan, W., Ba, J., Muller, T., Fang, G., Zhao, H., 2020. Rock physics model of tight oil siltstone for seismic prediction of brittleness. Geophys. Prospect. 68 (5), 1554–1574. https://doi.org/10.1111/1365-2478.12938.

Toksöz, M.N., Johnston, H.D., Timur, A., 1979. Attenuation of seismic waves in dry and saturated rocks: I. Laboratory measurements: Geophysics 44 (4), 681–690 org/10.1190/1.1440969.

Tucovic, N., Gegenhuber, N., 2017. Well-log based rock physics template of the Vienna Basin and the underlying Calcereous Alps. Acta Geophys. 65, 441–451.

Tutuncu, A.N., Podio, A.L., Sharma, M.M., 1994. An experimental investigation of factors influencing compressional- and shear-wave velocities and attenuations in tight gas sandstones. Geophysics 59 (1), 77–86.

Voigt, W., 1910. Lehrbuch der Kirstallphysik. Teubner.

Walderhaug, O., Eliassen, A., Aase, N.E., 2012. Prediction of permeability in quartz-rich sandstones: examples from the Norwegian continental shelf and the Fontainebleau sandstone. J. Sediment. Res. 82, 899–912. https://doi.org/10.2110/jsr.2012.79.

Xi, K., Cao, Y., Liu, K., Jahren, J., Zhu, R., Yuan, G., Hellevang, H., 2019. Authigenic minerals related to wettability and their impacts on oil accumulation in tight sandstone reservoirs: an example from the Lower Cretaceous Quantou Formation in the southern Songliao Basin, China. J. Asian Earth Sci. 178, 173–192.

Xiao, D., Jiang, S., Thul, D., Lu, S., Zhang, L., Li, B., 2018. Impacts of clay on pore structure, storage and percolation of tight sandstones from the Songliao Basin, China: implications for genetic classification of tight sandstone reservoirs. Fuel 211, 390–404.

Xu, S., Payne, M., 2009. Modeling elastic properties in carbonate rocks. Lead. Edge 28 (1), 66–74.

Yan, X., Yao, F., Cao, H., Ba, J., Hu, L., Yang, Z., 2011. Analyzing the mid-low porosity sandstone dry frame in central Sichuan based on effective medium theory. Appl. Geophys. 8 (3), 163–170.

Yu, H., Lu, X., Fu, W., Wang, Y., Xu, H., Xie, Q., Qu, X., Lu, J., 2020. Determination of minimum near miscible pressure region during CO_2 and associated gas injection for tight oil reservoir in Ordos Basin, China. Fuel 263 org/10.1016/j.fuel.2019.116737.

Zhang, L., Ba, J., Yin, W., Sun, W., Tang, J., 2017. Seismic wave propagation equations of conglomerate reservoirs: a triple-porosity structure model. Chin. J. Geophys. 60 (3), 1073–1087.

Zhang, L., Ba, J., Fu, L., Carcione, J.M., Cao, C., 2019. Estimation of pore microstructure by using the static and dynamic moduli. Int. J. Rock Mech. Min. Sci. 113, 24–30.

Zhou, X., Yuan, Q., Zhang, Y., Wang, H., Zeng, F., Zhang, L., 2019. Performance evaluation of CO_2 flooding process in tight oil reservoir via experimental and numerical simulation studies. Fuel 236, 730–746.